

“Bursts, Beats, and Beyond”: Uncovering the landscape from accretion to ignition of 4U 1728–34 using *AstroSat*

Anirudh Salgundi¹, Suman Bala^{2,1}, Gayathri Raman³, Utkarsh Pathak¹, Varun Bhalerao¹

¹ Department of Physics, Indian Institute of Technology Bombay, Powai, Mumbai 400076, India.

² Science and Technology Institute, Universities Space Research Association, Huntsville, AL 35805, USA.

³ Department of Astronomy and Astrophysics, The Pennsylvania State University, 525 Davey Lab, University Park, PA 16802, USA.

*Corresponding author. E-mail: anirudhsalgundi@gmail.com

Abstract. A comprehensive study on persistent and thermonuclear burst emission of 4U 1728–34, commonly known as ‘Slow Burster’ is performed using seven archival observations of *AstroSat* spanning from 2016–2019. The burst-free persistent spectra can be well fitted with a blackbody `bbbody` and a powerlaw `powerlaw` components, with a powerlaw photon index (Γ) was found to be ~ 2 indicating the source was in “high/soft” banana state or intermediate state. The time averaged power density spectrum reveals the presence of twin kilohertz Quasi Periodic Oscillations (kHz QPOs) with centroid frequencies 619 ± 10 Hz and 965 ± 6 Hz with a maximum fractional root mean squared amplitude of 6.24 ± 1.31 % at ~ 16 keV. From the upper kHz QPO, we infer the magnetospheric disk radius to be ~ 17 km, corresponding to a magnetic field strength of $0.35\text{--}1.27 \times 10^7$ G. The burst spectral evolution indicates Photospheric Radius Expansion (PRE) in five bursts, yielding a touchdown radius of 3.1–5.47 km. These bursts reached near-Eddington luminosities, through which the distance of the source was calculated to be 5.18–5.21 kpc. Two of the bursts show coherent oscillations at 362.81–363.93 Hz. The presence of twin kHz QPOs and coherent Burst Oscillations allows us to provide two different estimates for the spin frequency of the Neutron Star in the system, for the first time using *AstroSat*.

Keywords. stars: neutron — stars: oscillations — X-rays: binaries — X-rays: bursts — X-rays: individual: 4U 1728–34 — Quasi-Periodic Oscillations (QPOs)

1. Introduction

Low-Mass X-ray Binaries (LMXBs) are a class of binary systems that harbour a compact object either a Neutron Star (NS) or a Black Hole (BH) that accretes matter from a low mass ($\lesssim 1 M_{\odot}$) companion star. Accretion in these systems typically proceeds through Roche Lobe overflow. Depending on their spectral evolution properties, these systems are further classified into Atoll and Z sources (Hasinger & van der Klis, 1989). Atoll sources, in particular, transitions between what are known as low intensity ‘island’ state (or hard state) and high intensity ‘banana’ state (or soft state) based on the shape they trace on the colour-colour diagram. These state transitions have been associated with changes in mass accretion rate and evolution of the accretion flow (Hasinger & van der Klis, 1989). Unlike the Z class of sources, the Atoll source achieves maximum luminosities of $\leq 10\%$ L_{Edd} , varying less dynamically along the spectral state branches. The Neutron Stars (NS) in these systems are found to have

low surface magnetic fields ($\sim 10^8$ G).

Atoll sources are known to exhibit several types of time variability phenomena such as Quasi Periodic Oscillations (QPOs) and Thermonuclear Bursts (TNBs). QPOs are coherent signals observed in the Power Density Spectra, typically in mHz to kHz range. There is no consensus regarding the origin of the QPOs. They may originate due to the interaction between magnetosphere and the accretion flow at the innermost region of the accretion disk or due to relativistic effects near the NS surface (Wang, 2016). For several sources, the frequencies and amplitudes of these features are found to be correlated with the luminosity states (Ford et al., 2000), position in the Hardness Intensity Diagram (HID) (Wijnands & van der Klis, 1997), and even the spectral power law indices (Kaaret et al., 2002). Almost all Atoll sources also exhibit thermonuclear bursts. TNBs occur due to unstable nuclear burning of accreted material (predominantly composed of Hydrogen and Helium) on the surface of the NS (Bhattacharyya, 2010; Galloway et al., 2003). The

luminosities during these burst episodes can reach Eddington levels in a few seconds. The X-ray burst spectra of TNBs are typically characterized using blackbody emission. A small fraction ($\leq 20\%$) of these bursts exhibit rotational modulations of temperature variations, which are called ‘Burst Oscillations’ (BO). BOs are coherent, periodic variations in the burst flux. Their peak frequencies are associated with the NS spin frequency (Wijnands & van der Klis, 1998), thus making TNBs an important tool for probing NS spin.

The source, 4U 1728–34 (commonly known as the ‘slow burster’) is a persistent NS-LMXB that has been extensively characterized for over 5 decades using a number of X-ray telescopes. The NS nature of the compact object in this source was established soon after the detection of the first set of thermonuclear bursts using *SAS-3* and *Uhuru* (Hoffman et al., 1976; Kellogg et al., 1971; Lewin et al., 1976; Basinska et al., 1984). This LMXB is now known to host a weakly magnetized NS that is accreting from a Hydrogen poor companion (Shaposhnikov et al., 2003; Vincentelli & Uttley, 2023). Despite being a persistent Atoll source with no dramatic luminosity fluctuations, 4U 1728–34 exhibits a wide range of movement in its HID, where it transitions between soft and hard spectral states every ~ 40 –60 days (Munoz-Darias & Fender, 2014; Kong et al., 1998).

4U 1728–34 exhibits regular thermonuclear bursts which have been detected and characterized using *RXTE* (Strohmayer et al., 1996; Shaposhnikov et al., 2003), *XMM-NEWTON* (Wang et al., 2019), *INTEGRAL* (Falanga et al., 2006) and more recently, using *NICER* (Mahmoodifar et al., 2019) and *AstroSat* (Verdhan Chauhan et al., 2017) as well. There are more than 1100 bursts reported for this source (see the Multi Instrument Burst ARchive (MINBAR)¹ catalogue for most updated numbers; (Galloway et al., 2020)). The source distance, constrained using Eddington-limited Photospheric Radius Expansion (PRE) bursts, is around 4.4–5.1 kpc (Di Salvo et al., 2000; Galloway et al., 2003). The thermonuclear bursts from the 4U 1728–34 are usually short duration helium dominated bursts with typical burst recurrence time of ~ 3 hours (Vincentelli et al., 2020). Burst Oscillations (BO) at a frequency of ~ 361 –363 Hz have been reported for this source. The BO frequencies were typically found to increase as the burst evolved (van Straaten et al., 2001; Verdhan Chauhan et al., 2017; Franco, 2001). A recent study of the BO phenomenon using *NICER* reported an

unusually strong set of oscillations that had widely different properties in different energy bands (Mahmoodifar et al., 2019). This was the first bursting source where an infrared counterpart to a TNB was observed. The delay between the X-ray and IR burst emission has been used to constrain the orbital period of the system to be ≤ 3 hours at an inclination angle $\geq 8^\circ$ (Vincentelli et al., 2020; Vincentelli & Uttley, 2023).

4U 1728–34 exhibits strong aperiodic variability and millisecond-timescale Quasi-Periodic Oscillations (kHz QPOs), including twin kHz QPOs (Di Salvo et al., 2001; Méndez et al., 2001). The intriguing ‘parallel track’ behaviour between the lower kHz QPO and the X-ray intensity has been ascribed to bimodal accretion flows with contributions from disc and radial accretion (Wang & Zhang, 2020; Méndez et al., 2001).

The broadband X-ray spectrum for this source is described using a thermal comptonization model along with a blackbody component (for example, using *INTEGRAL*: (Falanga et al., 2006), *BeppoSAX*: (Di Salvo et al., 2000)). Additionally, the source has been observed to exhibit a strong reflection component (Mondal et al., 2017; Wang et al., 2019) in addition to a broad Fe line (see, for example, (Di Salvo et al., 2000; Tarana et al., 2011)).

AstroSat-LAXPC stands out as one of the few currently operational X-ray instruments, with high timing capabilities and broad spectral coverage, making it an ideal tool for investigating bursting sources and their properties. In this paper, we present a comprehensive analysis of several *AstroSat* observations of 4U 1728–34 and characterize the properties of the detected TNBs as well as the persistent emission.

The paper is organized as follows: In Section 2., we describe the observations and data reduction methods adopted. We present the data analysis methods and results in Section 3.. We summarize our results and discuss our findings in Section 4..

2. Observations and Data reduction

AstroSat is India’s first space-based multi-wavelength observatory, which is designed to perform simultaneous multi-wavelength observations ranging from far UV to hard X-rays. It consists of five sets of instruments, namely Ultra-violet Imaging Telescope (UVIT) (Tandon et al., 2017), Soft X-ray Telescope (SXT) (Singh et al., 2017), Large Area X-ray Proportional Counter (LAXPC) (Antia et al., 2017), Cadmium Zinc

¹<https://burst.sci.monash.edu/minbar/>

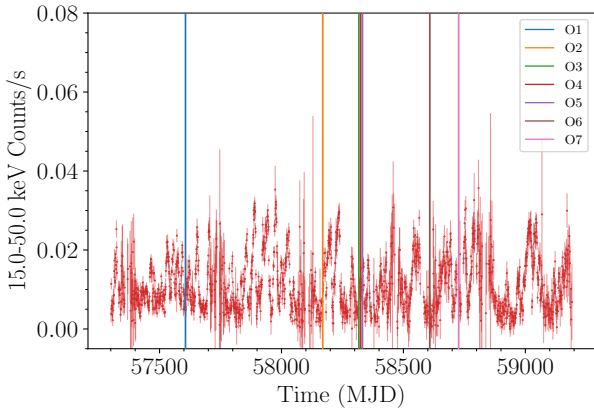


Figure 1: *Swift*-BAT daily lightcurve³ of 4U 1728–34 in the 15.0–50.0 keV energy range. The vertical line indicates epochs of *AstroSat* observations (O1–O7, in order) used for this work.

Telluride Imager (CZTI) (Bhalerao et al., 2017) and Scanning Sky Monitor (SSM) (Ramadevi et al., 2018) onboard the satellite.

For this study, we have utilized the archival observations of *AstroSat*² on 4U 1728–34 taken using LAXPC and SXT instruments between 2016–2019 (see Figure 1). A total of 13 thermonuclear bursts were detected in these observations. Further details regarding the observations are presented in Table 1.

2.1 SXT

SXT is an imaging and focusing telescope operating in soft X-rays between 0.3–8.0 keV. It has an effective area of approximately 90 cm² at ~1.5 keV, with a temporal resolution of ~2.4 s and a spectral resolution of ~150 eV at 6 keV in the Photon Counting (PC) mode. The level 1 SXT data were processed using the standard reduction pipeline AS1SXTLevel2-1.4b⁴ for each of the orbits and finally merged them using SXT merger tool SXTPYJULIAMERGER v01. The source image was extracted from the merged event file using XSELECT V2.5b from which the lightcurves and spectra were extracted. The background and response matrix files are provided by SXT Payload Operations Centre team. An off-axis Ancillary Response Files (ARF) was generated using the sxt_ARFModule tool

wherever necessary.

2.2 LAXPC

LAXPC is a cluster of three co-aligned proportional counters LAXPC-10, LAXPC-20 and LAXPC-30, that operates between 3.0–80.0 keV energy range with a total effective area of 6000 cm². It has an absolute temporal resolution of 10 μ s and a deadtime of 42 μ s (Antia et al., 2017). The level 1 LAXPC data were processed and background subtracted lightcurves and spectra were obtained using the standard data analysis tools LAXPCsoftware22Aug15, which is made available on *AstroSat* Science Support Cell (ASSC).⁵ Due to the gain instability caused by the gas leakage in LAXPC-10 since March 28, 2018 and LAXPC-30 not operational during some observations, data from LAXPC-20 was used to carry out spectral and temporal analysis for all the observations along with LAXPC-10 and LAXPC-30 for the observations where they were operational.

3. Data analysis and results

3.1 Persistent emission, Lightcurves and Hardness Intensity Diagram

The Good Time Intervals (GTIs) for LAXPC were obtained using `laxpc.make_stdgti`. The 3.0–80.0 keV lightcurves were then extracted using `laxpc.make_lightcurve`. O1, O4, O6, O7 show presence of thermonuclear bursts (see Table 4 for reference). In order to study the persistent emission, the GTIs were modified by removing the times when thermonuclear bursts were detected. The modified GTIs were used again to generate the burst-free lightcurves and spectra, which were later background subtracted. For SXT, a circular region of 15 arcmin radius was chosen and 0.4–6.0 keV lightcurves were extracted using standard XSELECT routines. For the observations where thermonuclear bursts were detected, the time segments were removed using `FILTER TIME` command in XSELECT. For LAXPC data, the 3.0–80.0 keV lightcurves were extracted using `laxpc.make_lightcurve` and the background was subtracted using the standard `laxpc.make_background` tool.

To track the spectral evolution, the hardness ratio was calculated from the LAXPC data, as the ratio of the count rates in the 3.0–5.5 keV and 5.5–30.0 keV bands. The HID was constructed using the

²https://astrobrowse.issdc.gov.in/astro_archive/archive/Home.jsp

³<https://swift.gsfc.nasa.gov/results/transients/GX354-0/>

⁴<http://astrosat-ssc.iucaa.in/sxtData>

⁵<http://astrosat-ssc.iucaa.in/laxpcData>

Table 1: Observation details of 4U 1728–34.

Observation ID	Start time (MJD)	Exposure (ks)		Mean count rates		Number of bursts
		SXT	LAXPC	SXT (0.6–7.0 keV)	LAXPC (3.0–80.0 keV)	
9000000578 (O1)	57606.36	13.26	64.70	9.42 ± 3.07	$472.02 \pm 21.73^{L1,2,3}$	1
9000001904 (O2)	58168.78	3.84	21.22	3.47 ± 1.86	478.57 ± 21.88^{L2}	0
9000002234 (O3)	58316.75	7.58	21.07	3.52 ± 1.88	383.39 ± 19.58^{L2}	0
9000002254 (O4) ^a	58324.11	–	108.20	–	261.38 ± 16.17^{L2}	2
9000002268 (O5)	58331.98	4.36	23.88	5.18 ± 2.28	281.95 ± 16.79^{L2}	0
9000002890 (O6)	58607.47	56.58	206.00	9.26 ± 3.04	274.61 ± 16.57^{L2}	5
9000003134 (O7)	58726.23	38.13	187.34	9.42 ± 3.07	353.40 ± 18.80^{L2}	5

^a SXT was not pointing at the source during O4, ^{L1,2,3} All three LAXPC detectors were used, ^{L2} only LAXPC20 was used.

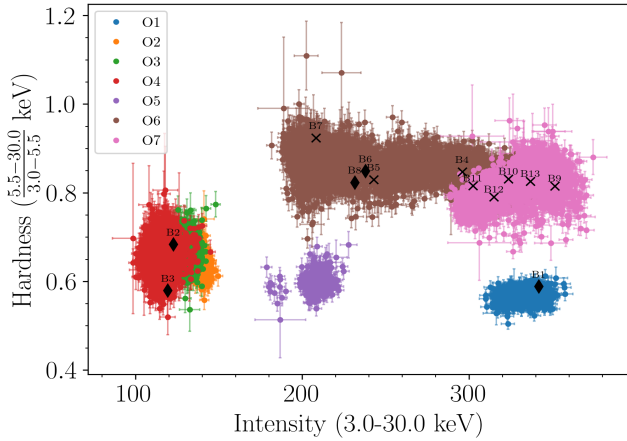


Figure 2: Hardness Intensity Diagram of 4U 1728–34 using LAXPC data. The markings are the positions in HID just before the bursts occurred. ‘♦’ represents PRE bursts and ‘x’ represents Non-PRE bursts.

hardness ratio and the 3–30 keV count rate. The HID was then divided into 25 s bins and the count rates were averaged in each bin.

From the HID, the hardness ratio varies between ~ 0.5 to ~ 1.0 and intensity (count rates) is varying between ~ 100 – 350 counts s^{-1} . We see thermonuclear bursts from 3 distinct regions of the HID. Region 1: where hardness is ~ 0.6 with high count rates ≥ 300 counts s^{-1} . This region has one burst observed (B1). Region 2: where the hardness ratio is ~ 0.6 with low count rates ≤ 120 counts s^{-1} where 2 bursts have been detected (B2 and B3). Region 3: where the hardness ratio is ≥ 0.8 and count rates ≥ 180 counts s^{-1} where 10 bursts have been detected (B4–B13).

3.2 Spectra

Spectral analysis of all the observations are carried out using the time averaged burst-free spectrum from SXT and LAXPC. For LAXPC, the energy range 4.0–25.0 keV is used for spectral studies due to large systematics below 4.0 keV and high background domination above 25.0 keV. For SXT, we have used 0.6–6.0 keV energy range for the spectral fitting. Due to poor data quality in some observations, the lower energy and upper energy limits for the SXT is chosen to be 0.9 keV, and 5.0 keV respectively. Further, occasionally SXT is known to show instrumental artefacts at ~ 1.8 keV and ~ 2.4 keV (Singh et al., 2017). For observations where the artefacts are found, the energy range 1.6–2.6 keV is excluded for analysis.

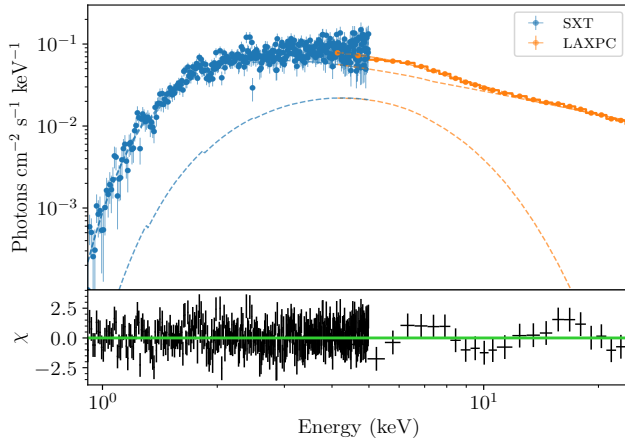
The GTIs from both LAXPC and SXT are logically ANDed using `ftmgttime` to obtain strictly simultaneous broadband spectra. The background spectrum for LAXPC is generated using `laxpc_make_backspectra`. For SXT, the background spectrum `SkyBkg_comb_EL3p5.C1_Rd16p0.v01.pha` is provided by AstroSat Science Support Cell (ASSC). We then perform joint spectral fitting for LAXPC and SXT using `XSPEC version: 12.13.0c` (Arnaud, 1996). A gain correction was applied to the SXT data with a fixed slope of 1 and varying offset, to account for the non-linear change in the detector gain. Further, a constant factor was also included for the SXT data to account for the differences in cross-calibration between the SXT and LAXPC instruments. Additionally, a systematic error of 3% was added to the data as prescribed by the *AstroSat* Payload Operations Center team (Bhattacharya, 2017).

The Tuebingen-Boulder ISM absorption model `tbabs` was used to account for the absorption by

Table 2: Best-fit parameters for the persistent time-averaged spectrum of all observations.

Model	Parameter	O1 0.6–25.0 keV	O2 0.9–25 keV	O3 0.9–25 keV	O4 4.0–25.0 keV	O5 0.9–25 keV	O6 ^a 0.6–25 keV	O7 0.9–25.0 keV
tbabs	N_H (10^{22} cm ⁻²)	$2.27^{+0.16}_{-0.15}$	$2.24^{+0.16}_{-0.12}$	$1.67^{+0.20}_{-0.17}$	2.50*	$2.41^{+0.14}_{-0.19}$	$1.91^{+0.07}_{-0.06}$	$2.12^{+0.13}_{-0.12}$
bbody	kT (keV)	1.87 ± 0.05	$1.32^{+0.05}_{-0.06}$	1.32 ± 0.05	$1.47^{+0.08}_{-0.07}$	$1.32^{+0.07}_{-0.05}$	1.46 ± 0.02	1.54 ± 0.05
	norm (10^{-2})	1.36 ± 0.06	$0.30^{+0.04}_{-0.05}$	$0.36^{+0.05}_{-0.04}$	0.27 ± 0.06	$0.44^{+0.09}_{-0.07}$	$1.31^{+0.05}_{-0.04}$	$1.50^{+0.08}_{-0.07}$
powerlaw	Γ	2.49 ± 0.03	$1.98^{+0.05}_{-0.04}$	1.88 ± 0.05	1.89 ± 0.07	$1.90^{+0.05}_{-0.06}$	$2.24^{+0.03}_{-0.04}$	2.35 ± 0.03
	norm	$1.42^{+0.13}_{-0.11}$	$0.26^{+0.04}_{-0.03}$	0.18 ± 0.03	$0.17^{+0.04}_{-0.03}$	$0.34^{+0.05}_{-0.06}$	0.48 ± 0.04	1.01 ± 0.07
$F_{p,bol}^1$	($\times 10^{-9}$ erg cm ⁻² s ⁻¹)	2.64 ± 0.02	1.12 ± 0.01	1.06 ± 0.01	0.96 ± 0.01	1.74 ± 0.01	1.82 ± 0.01	2.58 ± 0.02
\dot{m}/\dot{M}_{Edd}		0.136	0.058	0.055	0.049	0.090	0.094	0.133
$\chi^2/\text{d.o.f}$		1.43/436	1.07/427	0.84/406	1.20/21	1.07/476	1.24/501	1.20/405

^a up to energies up to 7.0 keV was used for this observation. For the rest of the observations, energies up to 6 keV have been used.

**Figure 3:** Joint spectral fit of the persistent emission of O2 using SXT (blue) and LAXPC (orange) data with the model combination `constant*tbabs*(bbody+powerlaw)`

the interstellar medium, which utilizes abundances and updated photoionization cross-sections (Wilms et al., 2000).

The best fit model for the persistent spectrum for all the observations is found to be `constant*tbabs*(bbody+powerlaw)`. The unabsorbed bolometric flux in the 3.0–30.0 keV energy range is calculated using the `flux` command. The best fit parameters along with 90% confidence errors for each of the observations are presented in Table 2. The Joint spectral fit along with the residuals are plotted for O2 in Figure 3, and for the rest of the observations are in Figure 11.

The blackbody temperature (kT) is found to be ~ 1.3 – 1.9 keV and the powerlaw photon index (Γ) is ~ 1.9 – 2.5 . The unabsorbed bolometric flux is found to vary between 0.96 – 2.64×10^{-9} erg cm⁻² s⁻¹,

which corresponds to ~ 5 – 13% of the Eddington mass accretion rate. O1 and O7 show higher fluxes, with accretion rates of $\sim 13\%$ of the Eddington rate. We do not see any disk reflection features around 6 keV in any of the observations.

3.3 Search for Quasi Periodic Oscillations

We carried out timing analysis using LAXPC data to search for quasi-periodic variability in the persistent lightcurve. We generated Root Mean Squared (RMS) normalized time averaged power density spectrum (PDS) from 10–2000 Hz using `laxpc.find_freqflag`. The PDS were geometrically binned by a factor of 1.02 in the frequency space using `laxpc.rebin_power`. The LAXPC software normalizes the fractional RMS power $(\text{RMS}/\text{mean})^2/\text{Hz}$ and subtracts out the poisson noise contribution, assuming a deadtime of 42 μs . This method is repeated for all the observations to investigate rapid X-ray variability. The time averaged power density spectrum of O1 shows the presence of twin kilohertz Quasi Periodic Oscillations (kHz QPOs) at 964 ± 6 Hz and 618 ± 10 Hz frequencies.

These frequencies are the centroid frequencies that were obtained by fitting a zero centred Lorentzian to the power density spectrum, which is given by:

$$L_\nu = \frac{r^2 \Delta\nu}{2\pi[(\frac{\Delta\nu}{2})^2 + (\nu - \nu_c)^2]} \quad (1)$$

Where $\Delta\nu$ is the full width at half maxima (FWHM), ν_c is the centroid frequency and r is the integrated RMS for the Lorentzian component. The best-fit parameters for the QPOs and 90% confi-

Table 3: Best-fit parameters for the time-averaged power density spectrum from 10–2000 Hz reported along with 90% confidence errors.

Model Component	Parameter	Value
1. Lorentzian	σ (Hz)	$33.27^{+4.04}_{-3.52}$
	ν_1 (Hz)	$20.28^{+0.98}_{-1.16}$
	Norm (10^{-3})	9.08 ± 0.01
2. Lorentzian	σ (Hz)	$125.93^{+32.11}_{-25.35}$
	ν_2 (Hz)	$110.18^{+8.61}_{-10.27}$
	Norm (10^{-3})	6.19 ± 0.01
3. Lorentzian QPO 1 (ν_l)	σ (Hz)	$81.84^{+38.71}_{-26.69}$
	ν_3 (Hz)	$618.65^{+9.80}_{-9.60}$
	Norm (10^{-3})	2.22 ± 0.01
4. Lorentzian QPO 2 (ν_u)	σ (Hz)	$123.62^{+19.01}_{-16.32}$
	ν_3 (Hz)	$964.54^{+5.84}_{-5.86}$
	Norm (10^{-3})	7.28 ± 0.01
$\Delta\chi^2/\text{dof}$		254.50/242.0

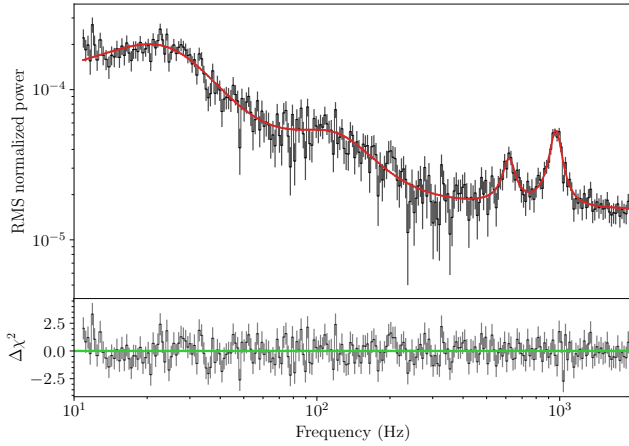


Figure 4: Time averaged power density spectrum of 10–2000 Hz of O1.

dence errors obtained are presented in Table 3. A total of four Lorentzian were required for adequately fitting the time averaged PDS. In order to quantify the coherence of the QPOs, we calculate the Q-factor ($\nu_c/\Delta\nu$), where ν_c is the centroid frequency and $\Delta\nu$ is the Full Width at Half Maxima, and identify QPOs where Q-factor > 2 . ν_l and ν_u together constitute twin kilohertz QPOs. These have been previously reported around similar frequencies by (Méndez et al., 2001; Di Salvo et al., 2001; Wang et al., 2018; Anand et al., 2024). No other observations showed presence of QPOs.

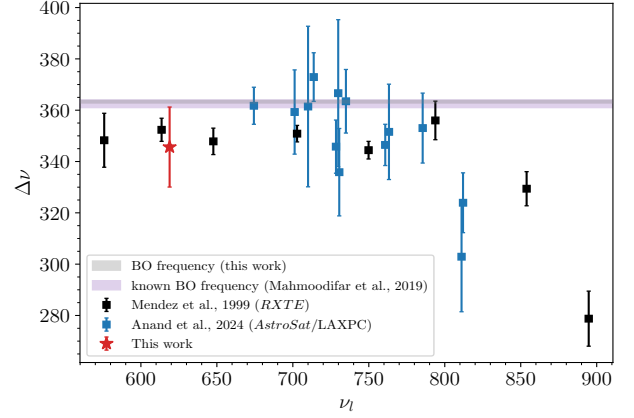


Figure 5: Difference in the upper and lower kHz QPO frequencies $\Delta\nu$ plotted against ν_l . The value of $\Delta\nu$ is smaller than the burst oscillation frequency (see Table 6)

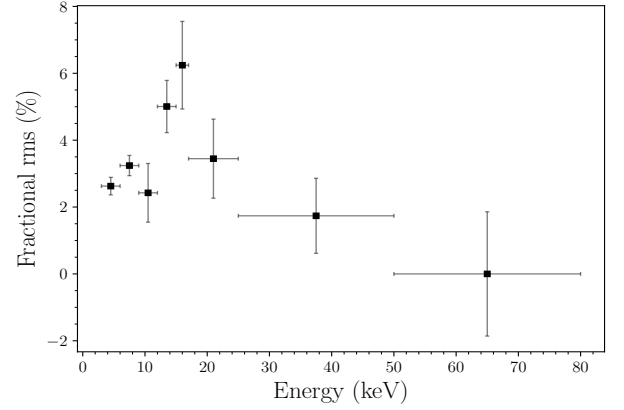


Figure 6: Time averaged RMS spectra of O1 showing the energy dependence of the upper kHz QPO.

3.4 Burst Emission and Lightcurves

In order to understand the energy dependence of the upper kHz QPO, we plot RMS as a function of energy (see Figure 6). From the RMS spectra, we see that the upper QPOs are strongest in the 14.0–16.0 keV energy range, with a peak fractional rms of $6.24 \pm 1.31\%$ at 16.0 ± 1.0 keV. We also see an increase in amplitude till ~ 16 keV, beyond which it starts decreasing. This may indicate that ~ 16 keV photons contributed relatively more in QPOs than other energy band photons.

We further characterize the difference between the upper and lower kHz QPO frequencies. Figure 5 is a plot representing, $\Delta\nu$ i.e. $\nu_u - \nu_l$ as a function of ν_l . The $\Delta\nu$ value is found to be 345.64 ± 15.59 Hz, which is smaller than the frequency of burst oscillation.

Table 4: Best-fit parameters of LAXPC 3.0–80.0 keV burst light curve fitting.

Burst	Peak Count rate counts s ⁻¹	Rise time (s)	Decay time (s)	t ₉₀ [*] (s)	PRE
B1	5962 ± 77	0.53 ± 0.11	6.08 ± 0.38	11.75 ± 0.39	y
B2	3838 ± 61	0.38 ± 0.14	4.59 ± 0.41	12.15 ± 0.43	y
B3	3756 ± 61	0.90 ± 0.17	6.02 ± 0.60	12.38 ± 0.62	y
B4	4398 ± 66	0.22 ± 0.03	6.58 ± 0.18	12.33 ± 0.18	n
B5	4726 ± 68	0.15 ± 0.12	6.93 ± 0.35	12.28 ± 0.37	n
B6	5594 ± 74	0.30 ± 0.04	5.57 ± 0.17	11.94 ± 0.17	y
B7	5404 ± 73	0.51 ± 0.10	5.04 ± 0.28	12.47 ± 0.30	n
B8	4684 ± 68	0.47 ± 0.05	4.88 ± 0.24	12.01 ± 0.24	y
B9	3932 ± 62	0.37 ± 0.08	6.19 ± 0.45	13.06 ± 0.46	n
B10	5570 ± 74	0.57 ± 0.08	4.80 ± 0.34	12.11 ± 0.35	n
B11	5588 ± 74	0.61 ± 0.10	4.36 ± 0.39	12.37 ± 0.40	n
B12	6230 ± 78	0.31 ± 0.11	5.99 ± 0.42	11.63 ± 0.43	n
B13	5822 ± 76	0.54 ± 0.11	5.74 ± 0.32	11.85 ± 0.34	n

* t₉₀ is a measure to quantify the duration during which 90% of the total burst energy (or counts) is emitted. .

tions seen in this source.

The observations O1, O4, O6 and O7 show the presence of a total of 13 thermonuclear bursts. The burst lightcurves are modelled using `mpfit`⁶ module which uses Levenberg-Marquardt least square minimization to fit the burst lightcurves. The best-fit burst parameters from the lightcurve are given in Table 4. While the observations O1 and O4 are located in region 1 and region 2 of the HID respectively, (see Figure 2), a total of 3 thermonuclear bursts (B1, B2 and B3) have been reported in these two observations. The peak count rate for B1 is ~ 6038 counts s⁻¹, while it is ~ 3700 counts s⁻¹ for bursts B2 and B3. Other parameters such as the burst duration, time taken to reach the peak count rate and decay rate are comparable for these three bursts. The Observations O6 and O7 belonging to region R3 in the HID shows a total of 11 thermonuclear bursts, with peak count rates ranging from ~ 3900 counts s⁻¹ (for B9) to ~ 6200 counts s⁻¹ (for B12), which is the highest peak count rate among all the bursts.

Burst B9 and B11, though located in the same region in the HID, show a drastic difference in the time taken to peak, i.e. ~ 2 s, and ~ 0.3 s, respectively. This contrast is also seen in burst duration. While B9 lasts for ~ 17 s, B11 lasts for ~ 10 s.

Energy resolved lightcurves of ~ 0.1 s are extracted in the energy ranges 3.0–9.0 keV (E1), 9.0–15.0 keV (E2), 15.0–21.0 keV (E3), 21.0–30.0 keV (E4) and 30.0–40.0 keV (E5). We observe that all the bursts show the presence of photons > 20 keV.

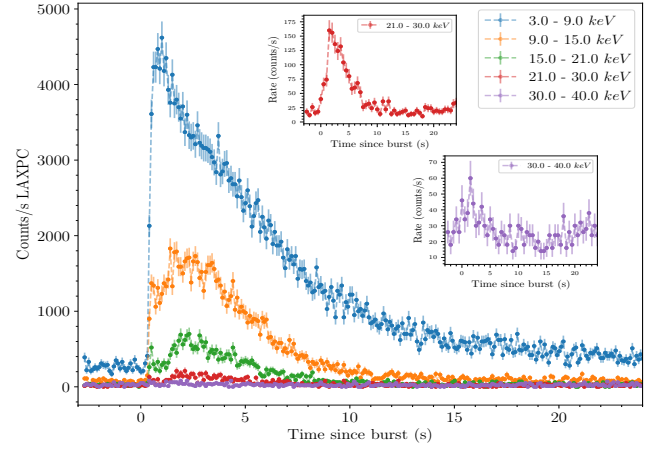


Figure 7: Energy resolved burst lightcurve for burst B12. The lightcurves of 21.0–30.0 keV and 30.0–50.0 keV energy range are shown separately, binned at 0.5 s.

In addition, the bursts except B4, B6 and B8 show photons of energy > 30 keV in the energy resolved lightcurves as seen in Figure 7. The energy resolved burst lightcurves of all the bursts are presented in Figure 13. This behaviour is further investigated using spectroscopy in Section 3.5.

3.5 Time resolved burst spectroscopy

We extract the LAXPC spectra for each of the bursts. The start time is considered as the time when the count rate exceeds the persistent emission by 10% of the peak count rate of the burst. To investigate the spectral evolution, consecutive spectra of 0.5 s from the start of the burst were extracted. The SXT instrument was not used for the analysis

⁶<https://github.com/segasai/astrolibpy/blob/master/mpfit/mpfit.py>

Table 5: Burst spectral parameters

Burst	kT_{peak}	$F_{peak,bol}$	R_{TD}	L/L_{Edd}	\dot{M}/\dot{M}_{Edd}
B1	2.70 ± 0.09	$5.94^{+0.09}_{-0.16}$	$4.70^{+0.10}_{-0.29}$	1.09	3.06
B2	2.91 ± 0.11	$3.55^{+0.09}_{-0.11}$	$3.49^{+0.09}_{-0.24}$	0.65	1.83
B3	3.09 ± 0.11	$3.38^{+0.08}_{-0.10}$	$3.18^{+0.08}_{-0.22}$	0.62	1.74
B4	2.47 ± 0.10	$3.37^{+0.06}_{-0.11}$	—	0.62	1.73
B5	2.61 ± 0.09	$4.21^{+0.07}_{-0.13}$	—	0.77	2.17
B6	2.65 ± 0.08	$5.48^{+0.10}_{-0.12}$	$5.54^{+0.10}_{-0.33}$	1.01	2.82
B7	$2.71^{+0.10}_{-0.09}$	$5.28^{+0.09}_{-0.16}$	—	0.97	2.72
B8	2.63 ± 0.10	$4.12^{+0.09}_{-0.12}$	$5.12^{+0.09}_{-0.35}$	0.76	2.12
B9	2.37 ± 0.10	$2.95^{+0.09}_{-0.08}$	—	0.54	1.52
B10	2.70 ± 0.09	$5.26^{+0.07}_{-0.16}$	—	0.97	2.71
B11	2.65 ± 0.08	$5.17^{+0.10}_{-0.15}$	—	0.95	2.66
B12	2.69 ± 0.08	$5.56^{+0.12}_{-0.15}$	—	1.02	2.86
B13	2.71 ± 0.08	$5.65^{+0.10}_{-0.16}$	—	1.04	2.91

kT_{peak} is the maximum temperature achieved during the burst, $F_{peak,bol}$ is the maximum bolometric flux attained during the burst (in $\times 10^{-9}$ erg cm $^{-2}$ s $^{-1}$), R_{TD} is the touchdown radius in km, L/L_{Edd} is the ratio of Source peak luminosity to Eddington luminosity L_{Edd} i.e. 1.76×10^{38} erg s $^{-1}$, \dot{M}/\dot{M}_{Edd} is the mass accretion rate at the peak of the burst relative to the Eddington limit \dot{M}_{Edd} i.e. 8.8×10^4 g cm $^{-2}$ s $^{-1}$. L_{Edd} and \dot{M}_{Edd} are calculated for a NS of mass $1.4 M_{\odot}$ and radius of 10 km (Galloway et al., 2008).

due to its larger time resolution of 2.37 s. Following several works such as (Mondal et al., 2017; Di Salvo et al., 2000; Falanga et al., 2006), we have used the persistent emission spectrum before or after the corresponding burst as the background spectrum in order to eliminate the contamination of burst-free photons.

For each interval of the time resolved burst spectra, we used XSPEC version: 12.13.0c (Arnaud, 1996) to fit the spectrum. We accounted for the interstellar medium absorption using the model **tbabs** and froze the N_H value to 2.5×10^{22} cm $^{-2}$ (Mondal et al., 2017) since we are not statistically capable of constraining this parameter using LAXPC.

Conventionally, burst spectra are fitted with a thermal blackbody model. We note here, that we do not adopt the variable flux (f_a) method, as we discuss later in Section 4.1, and we adopt the conventional method for the rest of this work. Figure 8 shows the evolution of burst spectral parameters.

We adopted a similar method as done by (Güver et al., 2012), for the identification of PRE bursts, estimating touchdown radius R_{TD} and touchdown flux R_{TD} . We infer that B1, B2, B3, B6, and B8 are indicative of PRE phenomena.

For bursts B11, B12, B13, the burst spectrum could not be fit sufficiently with just the **bbbodyrad** model⁷ for all the bins. We needed an additional

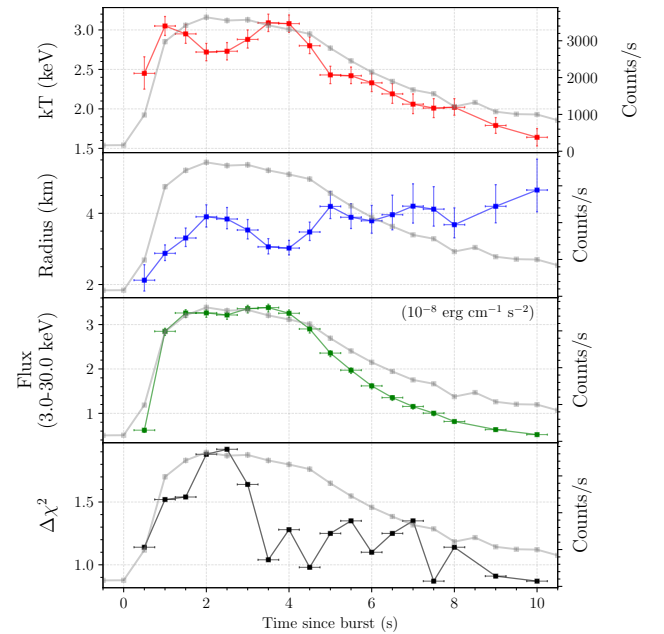


Figure 8: Evolution of spectral parameters of burst B2, elucidating PRE. The top panel shows the evolution of blackbody temperature kT (keV), second panel shows the evolution of blackbody radius R_{bb} (in km), third panel showing burst flux and bottom panel showing fit statistic

⁷The **bbbodyrad** model provides the blackbody colour tem-

powerlaw component to obtain a better statistically significant fit. In order to evaluate the improvement to the fit due to the addition of the powerlaw component, we calculate the F-statistic and its probability. Further, these 3 bursts showed counts >30.0 keV in the energy resolved lightcurves (see Figure 13). Details about the burst spectral parameters are presented in Table 5.

We calculated the bolometric flux F_{bol} using the relation given by (Galloway et al., 2008)

$$F_{bol} = 0.001076 N_{bb} (kT_{bb})^4 \text{ erg cm}^{-2} \text{ s}^{-1} \quad (2)$$

Since the inclination θ is not well constrained for this source, we calculate the luminosity assuming an isotropic emission using the relation $L = 4\pi R_{NS}^2 F_{bol}$. Assuming the accreted matter is evenly distributed on the surface of the NS and isotropic emission, the mass accretion rate per surface area is calculated using the below equation

$$\dot{M} = 6.7 \times 10^3 F_{bol}^* (1+z) \frac{D_{10}^2}{M_{NS}^* \times R_{NS}^*} \quad (3)$$

Where $(1+z) = \left(1 - \frac{2GM_{NS}}{R_{NS}c^2}\right)^{-1/2}$, and z is the gravitational redshift due to the neutron star's mass. F_{bol}^* is the bolometric flux in units of $\times 10^{-9} \text{ erg cm}^{-2} \text{ s}^{-1}$, M_{NS}^* and R_{NS}^* are the mass and radius of the neutron star in units of $1.4M_\odot$ and 10 km, respectively. All the calculations are presented in Table 5.

3.6 Search for Burst Oscillations

We used fast Fourier Transform (FFT) to search for oscillations in 10–1000 Hz frequency range in 3.0–30.0 keV energy range for 2 s window moving forward in steps of 0.5 s from the start of the burst. The power density spectrum for all the 13 bursts were generated using **Powerspectrum** package by **Stingray** library. The obtained Leahy normalized PDS, showed local maxima at ~ 362.85 Hz in B1, ~ 363.66 Hz in B4. B7, B10 and B11 showed a local maxima around the BO frequency, but were sub-threshold detections. All the obtained signals are in the tail region of the bursts, which may indicate coherent Burst Oscillations (see Figure 9).

In order to maximize the obtained power, we further extracted PDS in a 4 second window with

varying segment sizes of 1 s, 2 s and 3 s in a step of 0.1 s which accounts for $40+20+10 = 70$ overlapping segments, which in our case are considered as the total number of trials. The single trial chance probabilities and their significance have been calculated using the relation $x = e^{-P_{max}/2} \times n$, where P_{max} is the maximum Leahy power measured and n is the number of trials over which the detection was made and $X = \sqrt{2} \text{erf}^{-1}(1-x)$ where $X\sigma$ corresponds to detection significance. (see e.g. Roy et al. (2021)). Further, the fractional rms amplitudes are calculated using the relation:

$$A_{rms} = \left(\frac{P_s}{N_m}\right)^{1/2} \times \frac{N_m}{N_m - N_{bkg}} \quad (4)$$

where P_s is the power of the signal, N_m and N_{bkg} are total and background count rates during the interval searched. An approximate relation $A_{rms} = \sqrt{P_s/N_m}$ can be used, as N_{bkg} is negligible compared to high count rate (N_m) during the burst. The details of the burst oscillation candidates are presented in Table 6.

4. Discussion

4U 1728–34 is one of the most widely studied objects among the Atoll population. In this work, we analyse some additional properties of this system, using detailed timing and spectroscopic methods to better characterize this class of objects, as a whole. By correlating the burst properties, presence/absence of QPOs, and hardness diagrams, we derive several insights into the physical geometry of accretion powered systems.

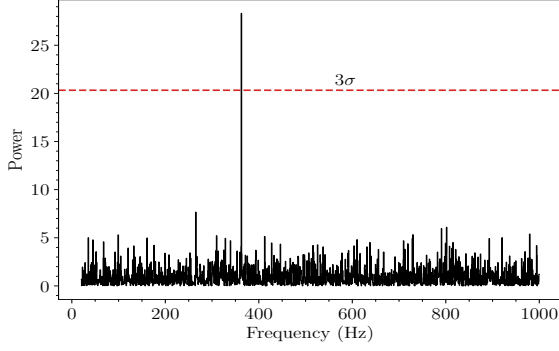
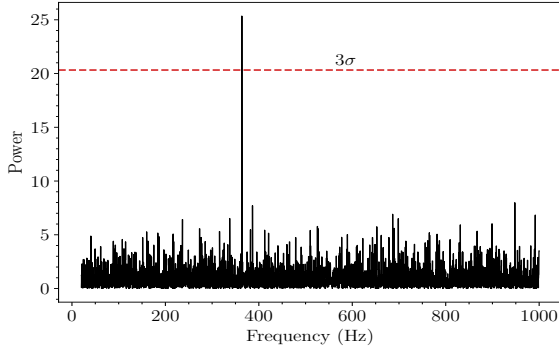
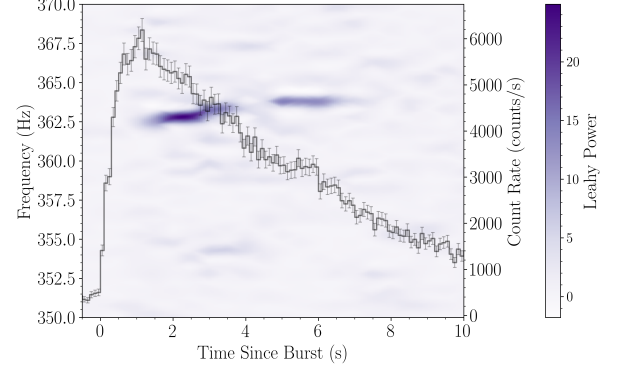
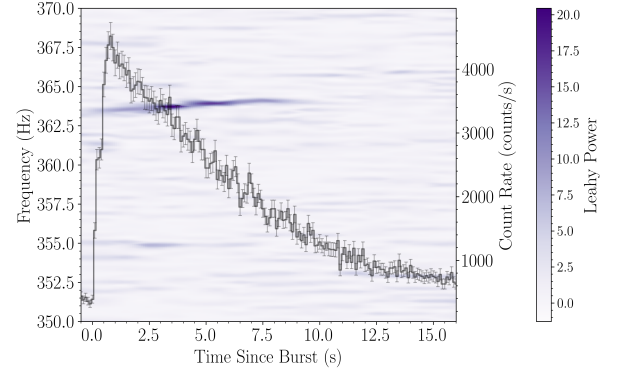
4.1 PRE bursts, touchdown fluxes and non-thermal burst emission

We adapt the method described by Güver et al. (2012) to identify the PRE bursts. Using the PRE bursts identified as part of this analysis, (B1, B2, B3, B6, and B8), we further infer the source distance (as described by Basinska et al. 1984), Eddington limits and compare them with previous estimates. Assuming a canonical NS radius of 10 km and a mass of $1.4 M_\odot$, we obtain a distance estimate of 5.18–5.21 kpc which is consistent with observations from *RXTE* (Galloway et al., 2008) and *NICER* (Bostanci et al., 2023). We further estimate the Eddington limit using the peak burst flux to be $\sim 1.46 \times 10^{38} \text{ erg s}^{-1}$. Using the bolometric flux obtained from the analysis of the persis-

perature (T_{bb}) and normalization ($N_{bb} = (R_{bb}/D_{10})^2$), where R_{bb} is the blackbody radius in km and D_{10} is the distance to the source in units of 10 kpc.

Table 6: Burst oscillation candidates

Burst	Frequency (Hz)	Single trial probability	Confidence level (σ)	Fractional rms (%)
B1	362.85	7.12×10^{-7}	4.06	3.12 ± 0.29
B4	363.73	3.12×10^{-6}	3.7	4.75 ± 0.47

**(a)** Power density spectrum of B1**(c)** Power density spectrum of B4**(b)** Dynamic power density spectrum of B1**(d)** Dynamic power density spectrum of B4**Figure 9:** Left: Power density spectrum; Right: Dynamic power density spectrum. Top: Burst Oscillations of B1; Bottom: Burst Oscillations of B4.

tent spectral fitting in Section 3.2, we infer that the source was accreting at 13.6% Eddington (for B1), 4.9% Eddington (for B2 and B3), 9.4% Eddington (for B6 and B8). The average bolometric flux $F_{peak,bol}$, during the peak of the bursts is found to be $\sim 4.6 \times 10^{-8} \text{ erg cm}^{-2} \text{ s}^{-1}$, which is smaller compared to the average peak flux of $9.4 \pm 3.6 \times 10^{-8} \text{ erg cm}^{-2} \text{ s}^{-1}$ in MINBAR (Galloway et al., 2020).

The continuum emission from thermonuclear bursts has been conventionally described using a simple blackbody, although several cases have observed deviations from a purely thermal spectrum (Bhattacharyya et al., 2018). For example, the scattering of the burst photons in the NS atmosphere can lead to the hardening of the spectrum (Bhattacharyya, 2010; Galloway & Keek, 2021). The re-

quirement of the non-thermal powerlaw component in three of the bursts, and the presence of hard photons ($>20 \text{ keV}$), in this work, is presumably a manifestation of such a comptonized effect. We note that a substantial subset of our bursts are observed in the high soft state of the source. A similar non-thermal component addition has been previously reported for 4U 1608–62 (Güver et al., 2021), although, in that case, the source was in the low-hard state.

Thermonuclear burst photons can in some cases lead to an increased accretion rate, which could increase the observed persistent emission (Bhattacharyya et al., 2018; Worpel et al., 2015). Alternatively, enhancements in the persistent emission near the burst can occur due to burst reprocessing in the accretion disk (in’t Zand et al., 2013). Whichever may be the case, it is becoming increasingly evident

that the burst emission affects the accretion process and could lead to variability in the persistent flux as measured during the burst. To deal with such a possibility, a new method called the “variable persistent flux method” (f_a -method, Worpel et al. 2013, 2015) has been developed. However, this method is a favourable fitting option for instruments sensitive to energies below 2 keV as it accounts for variability in the persistent emission during thermonuclear bursts, often influenced by reprocessing effects prominent in this energy range. Additionally, for the cases of 4U 1608–52, and XTE J1739–285, which have a large line of sight N_H absorption component, the use of scaling factor has not yielded any significant differences in the fitting process (Güver et al., 2021, 2022; Bult et al., 2021).

4.2 QPOs, Burst Oscillations and source state evolution

Some of the fastest timing signatures that are detected from accreting NS systems are the kHz QPOs ($\sim 100 \mu\text{s}$), which therefore serve as a direct probe of innermost accretion flows (van der Klis, 2000). The power spectral analysis of the burst-free light curve resulted in the detection of twin kHz QPOs at $619 \pm 10 \text{ Hz}$ and $965 \pm 6 \text{ Hz}$. Such a simultaneous detection of an upper and lower kHz QPO has been previously reported during several observations of 4U 1728–34 in the past (see for example., Di Salvo et al. 2001; Méndez et al. 2001). In addition, a series of QPO triplets (upper kHz, lower kHz and low frequency), detected using *AstroSat*, have been recently modelled using the Relativistic Precession Model (RPM) to constrain the mass and moment of inertia of the NS (Anand et al., 2024). Their work showed that, in general, the QPO measurements favoured stiffer Equations of State (EoS).

Typically, the upper kilohertz QPO frequency (ν_u) is assumed to be the Keplerian orbital frequency (ν_K) of the accretion plasma (Wang et al., 2018). It can be used to estimate the emission radius of the kHz QPOs, which can be considered the same as the magnetospheric disk radius (Lewin & van der Klis, 2006).

$$\nu_{ukhz} = \sqrt{\frac{GM}{4\pi^2 r^3}} \quad (5)$$

where G is the Gravitational constant, M is the mass of the NS and r is the emission radius of the kHz QPO referring to the NS centre i.e. the magnetospheric disk radius.

The co-rotation radius r_{co} in NS-LMXB is the

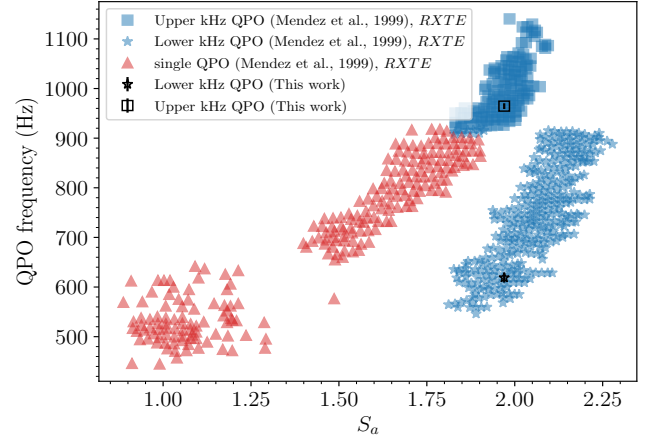


Figure 10: Frequencies of the upper and lower kHz QPOs plotted as a function of source position on the Hardness Intensity Diagram (S_a). Blue squares and * points represent lower and upper kHz QPOs respectively, and red data points are where only one QPO was observed. This figure is adapted from (Méndez & van der Klis, 1999).

radial distance referring to the NS centre where the accretion plasma co-rotates with the NS magnetosphere, meaning that the Keplerian orbital frequency ν_K there equals the NS spin frequency ν_s (Bhattacharya & van den Heuvel, 1991). Setting $\nu_K = \nu_s$ in Equation 5 gives the corotation radius r_{co} as

$$r_{co} = \frac{GM^{1/3}}{4\pi^2} \nu_s^{-2/3} \quad (6)$$

With the upper kHz QPO detected at $965 \pm 6 \text{ Hz}$, we obtain the co-rotation radius of $17.2 \pm 0.06 \text{ km}$. Assuming the dipolar magnetic field of NS and upper kHz QPO originated at the Alfvén radius, the magnetic field strength B_r at the magnetospheric disk radius ‘ r ’ is calculated as:

$$B_r = B_s (R_{NS}/r_m)^3 \quad (7)$$

Assuming $B_s \sim 1.8\text{--}6.5 \times 10^8 \text{ G}$ (Mondal et al., 2017), B_r is calculated to be $0.35\text{--}1.27 \times 10^7 \text{ G}$.

We compile a list of all previously detected high-frequency kHz QPOs using RXTE (Méndez et al., 2001) and *AstroSat*/LAXPC (this work) and indicate the peak frequencies as a function of the source spectral hardness S_a (see Figure 10). The twin kHz phenomenon is a consequence of the source being in the ‘banana’ state. The lower frequency further gets suppressed at lower accretion rates, consistent with

non-detections in the other observations analysed in our work. The absence of the upper kHz QPO frequency in lower accretion states observed with LAXPC, which was consistently detected in past *RXTE* observations, will be explored in future studies. The separation between the twin kHz QPO frequencies is typically found to be correlated in some form or the other to the NS spin frequency (for example, see Miller et al. 1998; Lamb & Miller 2001; Wijnands et al. 2003; Lee et al. 2004; Lewin & van der Klis 2006). The more commonly invoked beat frequency model (a.k.a. sonic-point model; Miller et al. 1998) suggests that the lower kHz QPO is observed at the beat frequency between the NS spin and the upper QPO due to the interaction of the neutron star’s magnetic field with matter at the inner edge of the disk.

BOs are established to be rotationally induced modulations that occur due to temperature variations on the NS surface (see Watts 2012 for a detailed review). The detection of a BO very close to the NS spin in the pulsar source SAX J1810.8–2609, firmly established the BO-spin frequency correlation (Wijnands & van der Klis, 1998). The ~ 363 Hz BO frequency of 4U 1728–34 has remained steady over the years and is consistent with our timing search results for bursts B1 and B4 bursts.

During the course of the seven *AstroSat* observations considered in this paper, 4U 1728–34 has evolved through several spectral states. The observations are separated by several years, O1 being the earliest (2016), while the remaining observations are from a later epoch, i.e., 2018 and 2019. As observed in almost all the Atoll sources, 4U 1728–34 also exhibits a variety of spectral and timing signatures during these epochs. Interestingly, the results from O1 stand out from the rest. During this particular observation period, the source is found to be in an extremely soft “banana” state, corresponding to a spectral powerlaw index of 2. Twin kHz QPOs are strongly detected in the power spectrum, with a peak-to-peak separation of around 346 Hz which is slightly lesser than the Burst Oscillations at 363 Hz found in the cooling tail of B1 (see Figure 9a), which belongs to the same observation. While the QPOs are found only during the start of the observation, the burst in the same observation is found much later. The simultaneous detection of kHz QPO and BO, allows us to further strengthen the association between the separation frequency, the BO and the NS fundamental spin frequency.

An important consequence of spectral state changes is that the variations in the accretion rate allows for sampling of the magnetospheric radius at

various radii. This can be effectively probed using kHz QPOs as has been demonstrated by Wang et al. (2018). A compilation of all the previous *RXTE* observations in various spectral states for 4U 1728–34 shows that the high/soft ‘banana state’ is where the field measurements are relatively stronger and the associated high frequency phenomena occur closer to the NS surface. This particular observation epoch (O1) samples a magnetic field strength of 2×10^7 G at a magnetospheric disk radius of 17 km.

Since we have a simultaneous detection of twin kHz QPOs and BO from the same observations, we have two independent handles for correlating these frequencies with the NS spin period. We indicate all the previous measurements of the difference between the twin kHz QPO frequencies (ν_{sep}) against the lower kHz QPO frequency (ν_l). In order to be consistent with the energy ranges, we compare all the *RXTE* and *AstroSat* measurements from Méndez et al. (2001) and Anand et al. (2024), respectively, with our observation now included. We plot the band of BO frequency values for comparison. We observe several interesting effects in Figure 5. While the BO frequencies occupy a very narrow range, the range of ν_{sep} has a lot more spread. Particularly, for the case of O1 which shows both the BO and the twin kHz QPOs, we observe that the separation frequency is slightly lower than the BO frequency, but is consistent within uncertainties. This allows us to better constrain kHz QPO correlation models. Our current observations strongly prefer the sonic-point beat frequency model, which interprets the difference to be close to the NS spin frequency. In addition to this, we observe a decreasing trend of ν_{sep} at larger ν_l . Such trends may hint towards an underlying physics that will be useful to better understand the origin of kHz QPOs.

4.3 Conclusions

We present a comprehensive study of the Atoll Source 4U 1728–34 using archival *AstroSat* observations. By performing detailed spectro-temporal studies of persistent emission and thermonuclear bursts, we have been able to derive several key insights into the physical properties of the source.

- From the Hardness Intensity Diagram, we observe the source to be in multiple intensity states. A total of thirteen thermonuclear bursts have been observed, with one burst in O1 and five bursts in O7, which belong to high intensity states. Five bursts were observed in O6 and two bursts in O5, which are intermediate and low intensity states respectively.

- O1 shows the presence of twin kHz QPOs, with a peak-to-peak separation of ~ 346 Hz, which is slightly smaller than the frequency of the reported Burst Oscillation (BO) at ~ 363 Hz. The presence of kHz QPOs and BO in the same observation allows us to better constrain the kHz QPO correlation models.
- The fractional rms of the upper kHz QPO increases with energy, and reaches a maximum amplitude of ~ 6 % around 16 keV. This indicates that the 16 keV photons are likely causing upper kHz QPO.
- From the upper kHz QPO frequency, we infer the magnetospheric disk radius to be ~ 17.2 km, and the magnetic field strength at the magnetospheric disk radius to be in the range of $0.35 - 1.27 \times 10^7$ G.
- The persistent spectra could be well described by a simple blackbody model, with the addition of a powerlaw component. The powerlaw spectral index Γ is found to be around ~ 2 for all the observations. No disk reflection features were observed.
- From the energy resolved burst lightcurves, we see that all of the thermonuclear bursts show the presence of photons > 20 keV. Some bursts show photons > 30 keV. The presence of hard photons in the burst emission is indicative of a non-thermal component in the burst emission.
- We infer that the source was accreting at 13.6 %, 4.9%, 9.4% and 13.3% of the Eddington limit during O1, O4, O6 and O7 respectively, where thermonuclear bursts are present. This suggests that the bursts are dominated by helium ignition after steady hydrogen burning via the CNO cycle.
- Among the 13 bursts, 5 bursts (B1, B2, B3, B6, and B8) were identified as PRE bursts. The touchdown radius is found to be in the range of 3.18–5.54 km. The source distance was estimated from the peak Luminosities to be 5.18–5.21 kpc. These measurements are consistent with previous observations.
- Coherent Burst Oscillations were detected in B1 and B4 at 362.85 Hz and 363.73 Hz respectively in the cooling tail of the bursts. The fractional rms amplitude of the Burst Oscillations was found to be 3.12 ± 0.29 % and 4.75 ± 0.47 % respectively.

5. Acknowledgements

We thank the Indian Space Research Organisation (ISRO) for financial support for the project “Timing and spectral studies of Type-1 thermonuclear X-ray bursts using AstroSat.” (DS 2B-13013(2)/3/2020-Sec.2 dtd. 12.01.2021). This work utilises data from LAXPC and SXT payloads onboard *AstroSat* made available through the Indian Space Science Data Center (ISSDC).

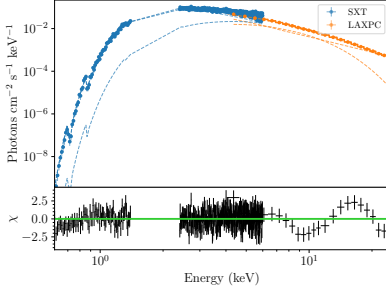
References

- Anand, K., Misra, R., Yadav, J. S., et al. 2024, *apj*, 967, 129
- Antia, H. M., Yadav, J. S., Agrawal, P. C., et al. 2017, *Journal of Astrophysics and Astronomy*, 38, 54
- Antia, H. M., Yadav, J. S., Agrawal, P. C., et al. 2017, *apjs*, 231, 10
- Arnaud, K. A. 1996, in *Astronomical Society of the Pacific Conference Series*, Vol. 101, *Astronomical Data Analysis Software and Systems V*, ed. Jacoby, George H. and Barnes, Jeannette, 17
- Basinska, E. M., Lewin, W. H. G., Sztajno, M., Cominsky, L. R., & Marshall, F. J. 1984, *Astrophysical Journal*, 281, 337
- Bhalerao, V., Bhattacharya, D., Vibhute, A., et al. 2017, *Journal of Astrophysics and Astronomy*, 38, 31
- Bhattacharya, D. 2017, *Journal of Astrophysics and Astronomy*, 38, 51
- Bhattacharya, D., & van den Heuvel, E. P. J. 1991, *physrep*, 203, 1
- Bhattacharyya, S. 2010, *Advances in Space Research*, 45, 949
- Bhattacharyya, S., Yadav, J. S., Sridhar, N., et al. 2018, *Astrophysical Journal*, 860, 88
- Bostancı, Z. F., Boztepe, T., Güver, T., et al. 2023, *Astrophysical Journal*, 958, 55
- Bult, P., Altamirano, D., Arzoumanian, Z., et al. 2021, *Astrophysical Journal*, 907, 79
- Di Salvo, T., Iaria, R., Burderi, L., & Robba, N. R. 2000, *apj*, 542, 1034

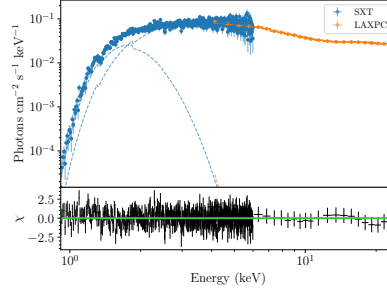
- Di Salvo, T., Méndez, M., van der Klis, M., Ford, E., & Robba, N. R. 2001, *apj*, 546, 1107
- Falanga, M., Götz, D., Goldoni, P., et al. 2006, *aap*, 458, 21
- Ford, E. C., van der Klis, M., & Kaaret, P. 2000, *Astrophysical Journal*, 537, 368
- Franco, L. M. 2001, *apj*, 554, 340
- Galloway, D. K., & Keek, L. 2021, in *Astrophysics and Space Science Library*, Vol. 461, *Timing Neutron Stars: Pulsations, Oscillations and Explosions*, ed. T. M. Belloni, M. Méndez, & C. Zhang, 209–262
- Galloway, D. K., Muno, M. P., Hartman, J. M., Psaltis, D., & Chakrabarty, D. 2008, *apjs*, 179, 360
- Galloway, D. K., Psaltis, D., Chakrabarty, D., & Muno, M. P. 2003, *Astrophysical Journal*, 590, 999
- Galloway, D. K., in’t Zand, J., Chenevez, J., et al. 2020, *apjs*, 249, 32
- Güver, T., Özel, F., & Psaltis, D. 2012, *Astrophysical Journal*, 747, 77
- Güver, T., Boztepe, T., Göğüş, E., et al. 2021, *Astrophysical Journal*, 910, 37
- Güver, T., Boztepe, T., Ballantyne, D. R., et al. 2022, *Monthly Notices of the Royal Astronomical Society*, 510, 1577
- Hasinger, G., & van der Klis, M. 1989, *Astronomy and Astrophysics*, 225, 79
- Hoffman, J., Marshall, H., Jernigan, G., & Li, F. 1976, *Astrophysical Journal*, 210, L13
- in’t Zand, J. J. M., Galloway, D. K., Marshall, H. L., et al. 2013, *Astronomy and Astrophysics*, 553, A83
- Kaaret, P., Zand, J. J. M. i. t., Heise, J., & et al. 2002, *Astrophysical Journal*, 575, 1018
- Kellogg, E. M., Gursky, H., & Leong, C. 1971, *Astrophysical Journal*, 169, L99
- Kong, A. K. H., Charles, P. A., & Kuulkers, E. 1998, *nat*, 3, 301
- Lamb, F. K., & Miller, M. C. 2001, *Astrophysical Journal*, 554, 1210
- Lee, W. H., Abramowicz, M. A., & Kluźniak, W. 2004, *Astrophysical Journal Letters*, 603, L93
- Lewin, L. M., Doty, J., & Clark, G. 1976, *IAU Circular*, 2922, 1
- Lewin, W. H. G., & van der Klis, M. 2006, *Compact Stellar X-ray Sources*, Vol. 39 (Cambridge University Press)
- Mahmoodifar, S., Strohmayer, T. E., Bult, P., et al. 2019, *apj*, 878, 145
- Méndez, M., van der Klis, M., & Ford, E. C. 2001, *apj*, 561, 1016
- Miller, M. C., Lamb, F. K., & Psaltis, D. 1998, *Astrophysical Journal*, 508, 791
- Mondal, A. S., Pahari, M., Dewangan, G. C., Misra, R., & Raychaudhuri, B. 2017, *mnras*, 466, 4991
- Munoz-Darias, T., & Fender, R. P. 2014, *Monthly Notices of the Royal Astronomical Society*, 443, 3270
- Méndez, M., & van der Klis, M. 1999, *Astrophysical Journal Letters*, 517, L51
- Ramadevi, M. C., Ravishankar, B. T., Sarwade, A. R., et al. 2018, *Journal of Astrophysics and Astronomy*, 39, 11
- Roy, P., Beri, A., & Bhattacharyya, S. 2021, *Monthly Notices of the Royal Astronomical Society*, 508, 2123
- Shaposhnikov, N., Titarchuk, L., & Haberl, F. 2003, *Astrophysical Journal*, 593, L35
- Singh, K. P., Stewart, G. C., & Westergaard, N. J. e. a. 2017, *Journal of Astrophysics and Astronomy*, 38, 29
- Strohmayer, T. E., Zhang, W., Swank, J. H., et al. 1996, *apjl*, 469, L9
- Tandon, S. N., Subramaniam, A., Girish, V., et al. 2017, *aj*, 154, 128
- Tarana, A., Belloni, T., Bazzano, A., Méndez, M., & Ubertini, P. 2011, *mnras*, 416, 873
- van der Klis, M. 2000, *Annual Review of Astronomy and Astrophysics*, 38, 717
- van Straaten, S., van der Klis, M., Kuulkers, E., & Méndez, M. 2001, *apj*, 551, 907

- Verdhan Chauhan, J., Yadav, J. S., Misra, R., et al. 2017, *apj*, 841, 41
- Vincentelli, F. M., Cavecchi, Y., Casella, P., et al. 2020, *mnras*, 495, L37
- Vincentelli, F. M., & Uttley, P. 2023, *Monthly Notices of the Royal Astronomical Society*, 525, 2509
- Wang, D.-H., & Zhang, C.-M. 2020, *mnras*, 497, 2893
- Wang, D.-H., Zhang, C.-M., & Qu, J.-L. 2018, *aap*, 618, A181
- Wang, J. 2016, *International Journal of Astronomy and Astrophysics*, 6, 82
- Wang, Y., Méndez, M., Altamirano, D., et al. 2019, *mnras*, 484, 3004
- Watts, A. L. 2012, *Annual Review of Astronomy and Astrophysics*, 50, 609
- Wijnands, R., & van der Klis, M. 1997, *Astrophysical Journal*, 482, L65
- Wijnands, R., & van der Klis, M. 1998, *Nature*, 394, 344
- Wijnands, R., van der Klis, M., Homan, J., et al. 2003, *Nature*, 424, 44
- Wilms, J., Allen, A., & McCray, R. 2000, *The Astrophysical Journal*, 542, 914
- Worpel, H., Galloway, D. K., & Price, D. J. 2013, *Astrophysical Journal*, 772, 94
- . 2015, *Astrophysical Journal*, 801, 60

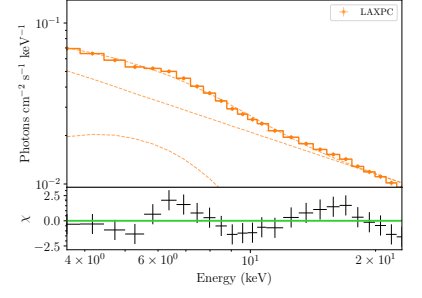
6. Appendix



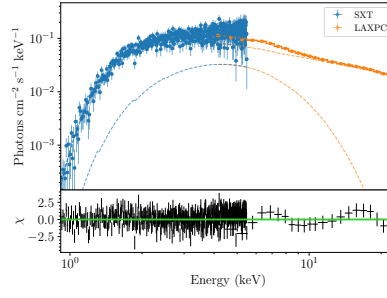
(a) Same as Figure 3, for O1



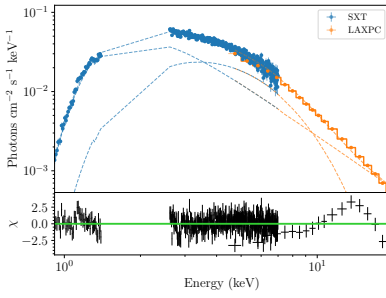
(b) Same as Figure 3, for O3



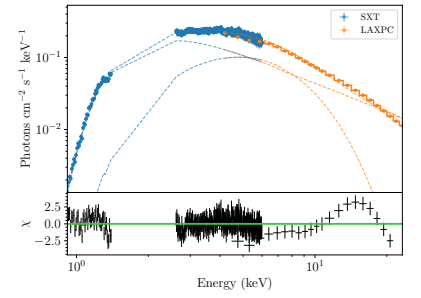
(c) Same as Figure 3, for O4



(d) Same as Figure 3, for O5

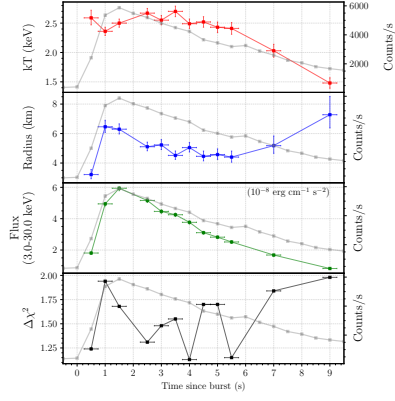


(e) Same as Figure 3, for O6

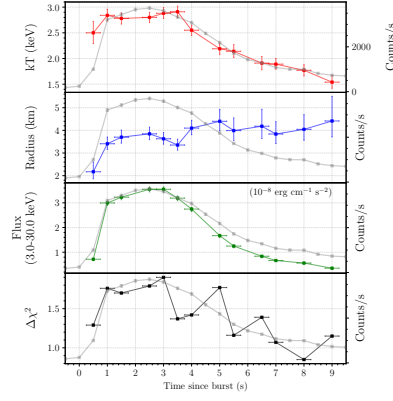


(f) Same as Figure 3, for O7

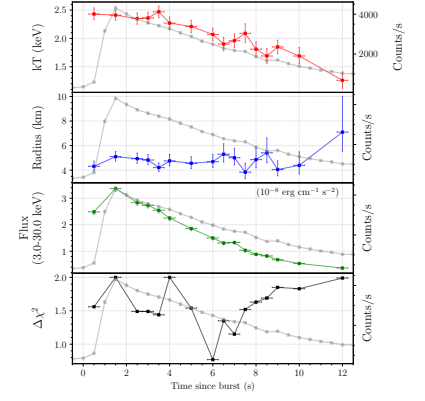
Figure 11: Joint spectral fit



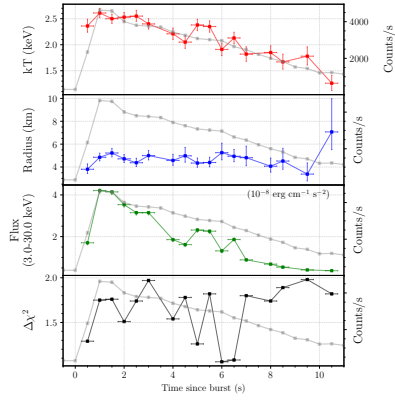
(a) Same as Figure 8, for B1



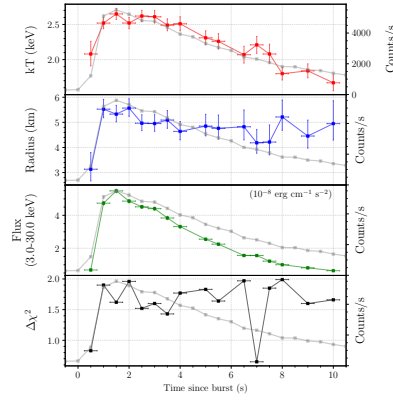
(b) Same as Figure 8, for B2



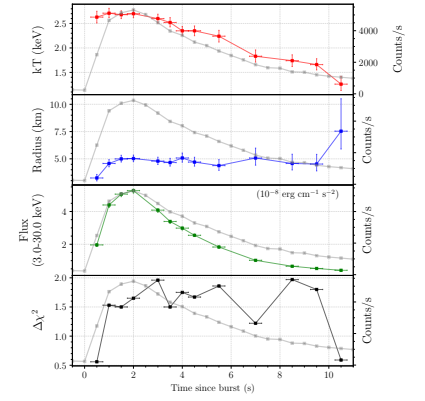
(c) Same as Figure 8, for B4



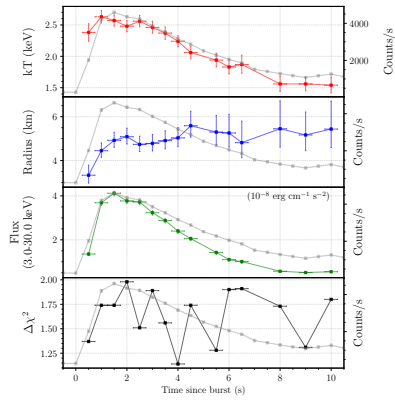
(d) Same as Figure 8, for B5



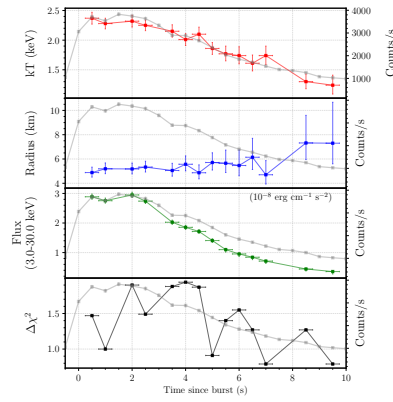
(e) Same as Figure 8, for B6



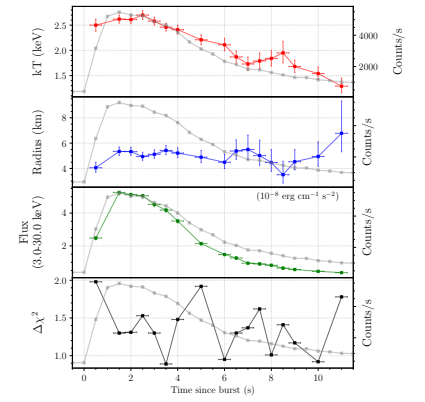
(f) Same as Figure 8, for B7



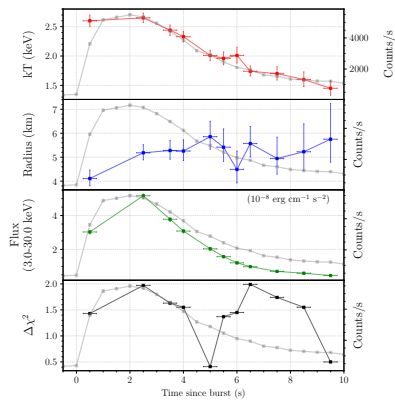
(g) Same as Figure 8, for B8



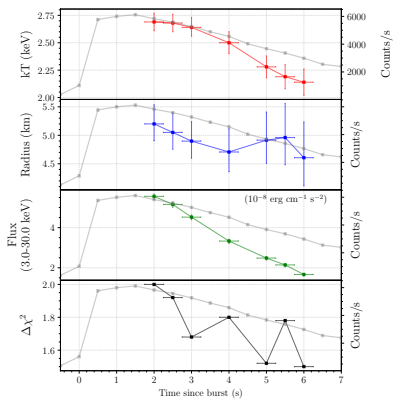
(h) Same as Figure 8, for B9



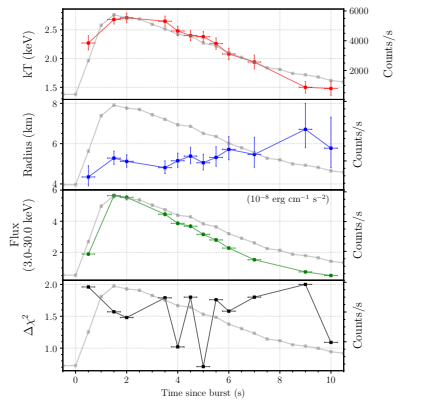
(i) Same as Figure 8, for B10



(j) Same as Figure 8, for B11

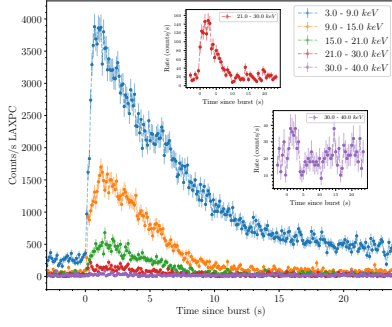


(k) Same as Figure 8, for B12

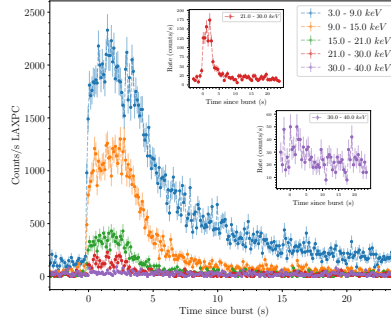


(l) Same as Figure 8, for B13

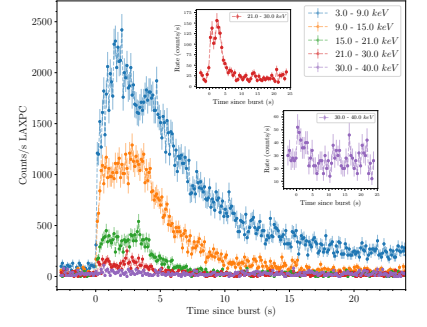
Figure 12: Set of 12 burst parameter images (B3).



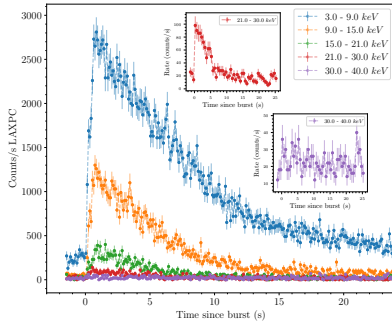
(a) Same as Figure 7, for B1



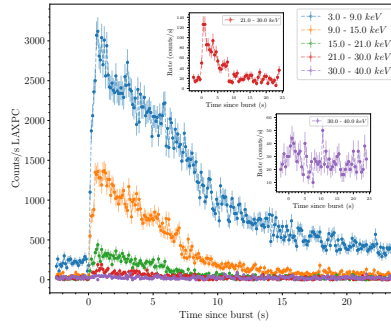
(b) Same as Figure 7, for B2



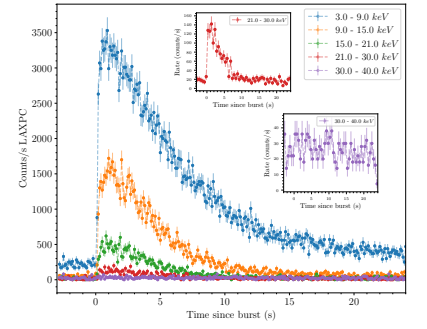
(c) Same as Figure 7, for B3



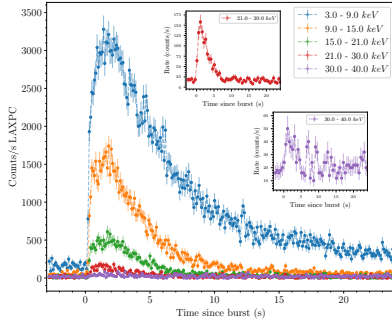
(d) Same as Figure 7, for B4



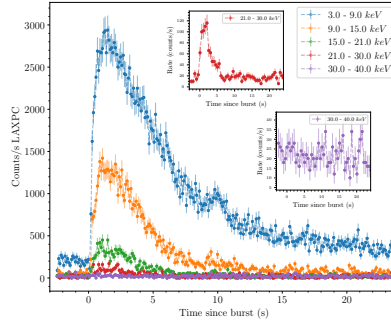
(e) Same as Figure 7, for B5



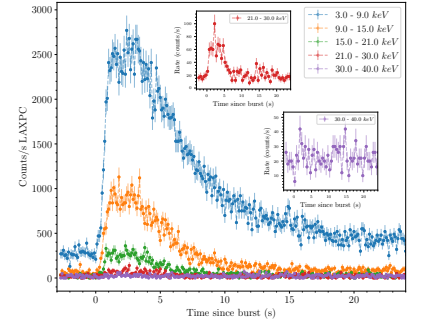
(f) Same as Figure 7, for B6



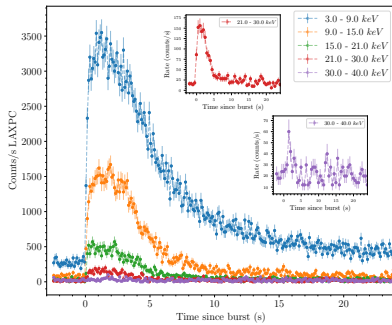
(g) Same as Figure 7, for B7



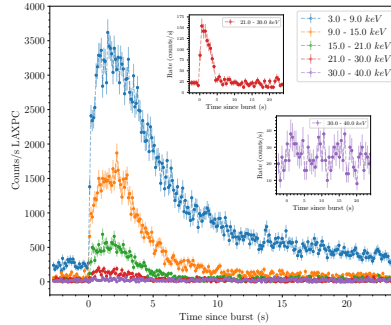
(h) Same as Figure 7, for B8



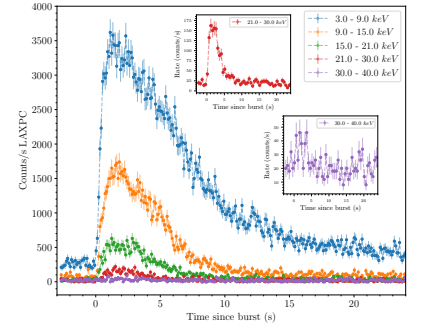
(i) Same as Figure 7, for B9



(j) Same as Figure 7, for B10



(k) Same as Figure 7, for B11



(l) Same as Figure 7, for B13

Figure 13: Energy resolved burst lightcurves